Electron microprobe chemical dating of uraninite as a reconnaissance tool for leucogranite geochronology

José M. Hurtado, Jr. *
Nilanjan Chatterjee
Jahandar Ramezani
Kip V. Hodges **
Samuel A. Bowring

Department of Earth, Atmospheric, and Planetary Sciences, Massachusetts Institute of Technology, Cambridge, Massachusetts 02139

* Corresponding author (now at the University of Texas at El Paso)
Address: UTEP, Department of Geological Sciences, room 319, 500 University Blvd., El Paso, Texas 79902
Email: hurtado@geo.utep.edu

** Now at the School of Earth and Space Exploration, Arizona State University

ABSTRACT

We suggest that electron microprobe techniques may be employed to date Tertiary samples of uraninite (UO_2), which can contain very high concentrations of radiogenic Pb after only a few million of years of U and Th decay. Although uraninite is regarded as a rare accessory mineral, it is relatively abundant in leucogranitic rocks such as those found in the Himalayan orogen. We apply the U-Th-total Pb electron microprobe chemical dating method to a uraninite crystal from a ca. 18.3 Ma dike of the Mugu granite from the Upper Mustang region of central Nepal. With this technique, we calculate a mean chemical date that is consistent with isotope-dilution thermal ionization

mass spectrometry (ID-TIMS) U-Pb dates obtained from seven other uraninite grains and a monazite crystal from the same sample. Electron microprobe chemical dating yields results that typically will be an order of magnitude less precise than conventional dates: in the specific case of the Mugu granite, single point chemical dates each have ca. 1.5 Ma 2σ (95%) confidence level uncertainties. However, the mean chemical date of 15 point analyses of the crystal we study has a 2SE (2 standard error) uncertainty of ca. 400 ka, comparable to uncertainties obtained with ID-TIMS. These results show that electron microprobe chemical dating of uraninite has substantial promise as a reconnaissance tool for the geochronology of young granitic rocks. The electron microprobe work also reveals substantial chemical complexity within uraninite that must be taken into account. The analyzed crystal displays a texturally and chemically distinctive core and rim that suggests episodic growth. Concentration gradients in U, Th, and Y across the boundary imply diffusive modification with $D_{nU} \approx D_{nTh} \approx \frac{1}{2} D_{nY}$. We estimate the diffusivity of U, Th, and Y in uraninite at ca. 700 °C to be > 10^{-7} cm^2 s^{-1}. In contrast, Pb shows no distinctive concentration gradient across the core-rim boundary, implying that Pb has a much higher diffusivity in uraninite than U, Th, or Y. We estimate that Pb loss of as much as ca. 8.9% has occurred in the uraninite grains we analyzed by ID-TIMS.

KEYWORDS: uraninite, electron microprobe, chemical dating, Himalayan leucogranite

INTRODUCTION

Leucogranitic rocks produced by crustal melting are frequently found in collisional orogenic settings and have the potential to provide important constraints on the absolute ages of deformational events that occurred during anatexis. Various studies [as reviewed by 1] have demonstrated spatial and temporal relationships between anatexis and both contractional and extensional deformation in the Himalayan orogen. High-precision U-Pb geochronology of pre-, syn-, and post-kinematic granites utilizing isotope-dilution, thermal-ionization mass spectrometry (ID-TIMS) has proved to be a powerful tool for unraveling the complex geologic history of the Himalaya [e.g. 2, 3-6]. However, the existence of numerous generations of anatexites in the Himalaya and the complexity of accessory mineral suites in these rocks [e.g. 7] requires painstaking, systematic effort for ID-TIMS geochronology to be effective. It is therefore useful to explore reconnaissance methods of U-Pb geochronology that, while inherently less precise, might better inform and facilitate detailed ID-TIMS work.

One reconnaissance method that has been used to great effect in the Himalaya is Th-Pb ion microprobe isotopic dating of monazite [8-12]. A second, high spatial resolution, reconnaissance approach to dating monazite employs chemical rather than isotopic data. This method presumes that essentially all Pb in monazite is derived from the *in situ* decay of U and Th, such that the concentration of Pb in a specific sample is proportional to its age [13]. For monazites that are sufficiently old – typically Paleozoic or older – the necessary measurements can be made with electron microprobe equipment, instruments that are more widely available than ion microprobes and that provide an order-of-magnitude better spatial resolution than is commonly realized in most ion

microprobe studies. Although electron microprobe chemical dating of monazite has proved to be an important tool for tectonic studies in older orogenic settings [e.g. 14], the concentrations of radiogenic Pb in Tertiary monazites – such as those found in the Himalaya – are sufficiently low to limit usefulness of the technique using currently available technology. Another common leucogranite accessory mineral – uraninite (UO_2) – should have higher Pb concentrations due to its high U concentration, and has been used with success for Paleozoic and older samples [15-18]. In this paper, we show that uraninite can be a useful target for electron microprobe chemical dating studies of young samples.

THEORY

The radioactive decay of ^{235}U, ^{238}U, and ^{232}Th produces ^{207}Pb, ^{206}Pb, and ^{208}Pb, respectively. If a mineral incorporates no common Pb at the time of crystallization, the concentration of Pb after an elapsed time (t) is due solely to the radioactive parent U and Th isotopes and is governed by the composite decay equation:

$$C_{Pb} = C_{Th}\left[0.897\left(e^{\lambda_{232}t} - 1\right)\right] + C_{U}\left[0.859\left(e^{\lambda_{238}t} - 1\right) + 0.006\left(e^{\lambda_{235}t} - 1\right)\right] \quad (1),$$

where C_{Pb}, C_{Th}, and C_U are concentrations (in ppm) of Pb, Th, and U, respectively; λ_{232}, λ_{238}, and λ_{235} are the decay constants (in yr^{-1}) for ^{232}Th, ^{238}U, and ^{235}U, respectively [19]; and t is age (in yr). The coefficient preceding the first exponential term in equation (1) is the mass ratio of ^{208}Pb to ^{232}Th (i.e. $208/232 \approx 0.897$); the coefficients preceding the second and third exponential terms are the ratios of the abundance fractions of the respective U isotopes to the mean atomic mass of U (i.e. $0.9928/238.04 \approx 0.859$ for ^{238}U;

$0.0072/238.04 \approx 0.006$ for ^{235}U). An iterative solution to equation (1) forms the basis for published electron microprobe chemical dating studies of monazite [e.g. 13, 14, 20, 21].

APPLICATION TO LEUCOGRANITE FROM THE NEPAL HIMALAYA

We illustrate the use of this approach with uraninite from a sample of Himalayan leucogranite collected in the Upper Mustang region of north central Nepal (Figure 1). The northwestern flank of a major N-S rift in this region – the Thakkhola graben – consists of a metamorphic massif dominated by exposures of Mesozoic siliciclastic and carbonate rocks metamorphosed to greenschist and amphibolite facies during the Tertiary. These rocks are intruded by two suites of granites: porphyritic to megacrystic granite of the Mustang pluton; and fine- to medium-grained, more leucocratic bodies of the Mugu leucogranite [22]. Based on their field relationships with respect to deformational fabrics, it appears that the Mugu leucogranites represent several distinctive episodes of anatectic melting. Previously published Th-Pb [10] and recently obtained ID-TIMS U-Pb dates for accessory minerals [23] demonstrate that the Mugu leucogranites range from > ca. 20.76 Ma to at least ca. 17.6 Ma.

The particular sample of Mugu granite we examine, 00KG20, was collected from a late-phase, 0.5 m-wide dike that intrudes both an earlier Mugu granite dike and dark, calc-pelitic metamorphosed country rock (Figure 2a). In addition to monazite, the accessory mineral suite for this sample included relatively abundant, black, euhedral crystals of uraninite (Figure 2b). Pure accessory mineral separates were obtained from a crushed aliquot of 00KG20 using standard magnetic and gravimetric separation techniques. One uraninite crystal from 00KG20 (u5) was selected for electron microprobe chemical dating, while seven other uraninite grains (u1-u3 & u4a-d) were

dissolved for comparative ID-TIMS geochronology. Two monazites from 00KG20 (m1 & m2) were also measured with ID-TIMS.

Electron Microprobe Analytical Methods

Crystal u5 is a cubic crystal approximately 200 μm across. We mounted it in epoxy, and we ground and polished the mount to expose a rectangular cross section through the core of the crystal. The polished section was then washed with ethanol and carbon-coated for electron microprobe analysis at the Massachusetts Institute of Technology with a JEOL JXA-733 instrument. Back-scattered electron (BSE) and secondary electron (SE) images of the grain (Figure 2c & d, respectively) were produced in order to qualitatively evaluate the extent of compositional zoning and as an aid to selecting spots for quantitative analysis. Energy dispersive spectrometry (EDS) analyses were also performed on inclusions within the grain to identify their mineralogy. Quantitative point measurements of U, Th, Pb, and Y concentrations were made along two core-to-rim transects of grain u5 (Figure 2c & d): Transect 1 (circles), which comprises 14 semi-equally-spaced spot analyses, and Transect 2 (crosses), which comprises 10 spots. This approach was chosen in order to evaluate the magnitude of chemical zoning in the grain. This is valuable information since gradients in U, Th, and Pb concentrations can result in spatial variations in calculated chemical dates.

The quantitative point analyses were performed by wavelength dispersive spectrometry (WDS) using PET diffracting crystals and sealed Xe-proportional counters. Prior to quantitative analysis, the WD spectrometers were calibrated with respect to U, Th, Pb, and Y using UO_2, ThO_2, $ThSiO_4$, $PbTiO_3$, and YAG (Y-Al-garnet: $Y_3Al_5O_{12}$)

standards. All measurements were made with an accelerating voltage of 20 kV, a beam current of 100 nA, and a dwell time of 240 seconds per measured element in order to maximize analytical precision. The minimum detection limits under these conditions were ca. 525 ppm for U, ca. 151 ppm for Th, ca. 273 ppm for Pb, and ca. 263 ppm for Y. The spot size was ca. 1 μm. The X-ray lines used for concentration measurements were PbM_β, ThM_β, UM_β, and YL_α. Matrix corrections were performed with the CITZAF program [24] using the atomic number correction of Ducumb and Reed [25], tabulated mass absorption coefficients [26], and the fluorescence correction of Reed [27].

Concentrations of U, Th, and Pb in grain u5 were measured simultaneously using three different WD spectrometers equipped with PET diffracting crystals. We measured PbM_β and ThM_β sequentially with the best WD spectrometer. The other two WD spectrometers were used to simultaneously measure UM_β and YL_α. After each measurement, the *k*-ratios for U and Pb were corrected for spectral interferences from the overlapping ThM_β and YL_α lines, respectively [e.g. 13, 20, 21]. This was done by measuring the x-ray intensities of ThM_β in the U-free $ThSiO_4$ standard and of YL_α in the Pb-free YAG standard. These measurements, scaled by multiplying by the *k*-ratios of Th and Y in grain u5, were subtracted from the measured intensities of U and Pb in grain u5 to yield corrected U and Pb intensities. We find that Th interference creates an average U content overestimate of ca. 16 ppm, and Y interference creates an average Pb content overestimate of ca. 35 ppm. Oxygen concentrations were calculated from stoichiometry of the oxides of U, Th, Pb and Y. We assume that there is negligible common Pb [15] and that mass transfer has not significantly altered the elemental concentrations in the uraninite [e.g. 13, 21] and use the U, Th, and Pb concentrations and equation (1) to

calculate U-Th-total Pb chemical dates. Uncertainties in the dates were estimated by propagating analytical uncertainties in U, Th, and Pb concentrations through equation (1) using a modified Monte Carlo method [20, 28, 29], and, for individual points, they are reported at the 2σ (95%) confidence level. The uncertainties do not include geologic uncertainty or uncertainty in the calibration standards, although according to Montel [13] the latter only contributes ca. 1% to the total uncertainty. Concentration data and calculated chemical dates are given in Table 1.

Grain Characteristics

When uraninite crystals from 00KG20 are examined under a binocular microscope, their crystal faces display a specular patina that suggests the presence of microinclusions (Figure 2b). BSE and SE imagery of grain u5 confirm the presence of abundant inclusions, many of which were plucked during sample polishing, leaving a large number of pockmarks and voids on the surface (Figure 2c & d). Some of the void space left by excavated inclusions forms a conspicuous, 8 μm wide, octahedrally-symmetric, concentric band that has the form of crystal faces (Figure 2c & d). EDS analyses demonstrate that many of the inclusions still remaining in the grain are quartz, although a few were found to be fayalite, aluminosilicate, and diopside. Aluminosilicate and diopside both occur in the calc-pelitic country rocks of Upper Mustang (and specifically in the host rock to 00KG20) so the inclusions are therefore regarded as xenocrystic. The presence of fayalite and diopside inclusions in u5 is petrologically significant because xenocrystic diopside would be expected to dissolve quickly in a leucogranitic magma.

ID-TIMS Analytical Methods

For comparison with the electron microprobe chemical dates, we selected four euhedral, cubic uraninite crystals (u1-u4) ranging in size from 75 μm to 150 μm on a side (Figure 2b) for conventional U-Pb analysis. We fractured grain u4 and selected four pieces (u4a-d) for individual analyses. The seven grains selected for analysis were photographed and measured using a binocular microscope with calibrated reticule and video display in order to estimate their weights. Experience in our facility suggests that the estimated values have a nominal error of roughly 20%. Prior to analysis, the grains were thoroughly washed in de-ionized water in an ultrasonic bath on a hot plate. Grains u4a and u4b were washed briefly in 4N HNO_3 at 80 °C. Washed and rinsed grains were loaded into FEP Teflon® microcapsules, spiked with a mixed ^{205}Pb-^{233}U-^{235}U tracer solution, and dissolved in concentrated HF at 220 °C within pressure vessels for 48-60 hours. Dissolution was followed by conversion to chloride form using 6N HCl at 180 °C for 12 hours. Pb and U were isolated and extracted from the samples using a miniaturized HCl-based anion-exchange chromatography procedure modified after Krogh [30]. U and Pb were then loaded separately on single, degassed Re filaments with a silica gel-H_3PO_4 emitter solution. Isotopic compositions were measured by isotope-dilution, thermal-ionization mass spectrometry (ID-TIMS) on a VG Sector 54 multi-collector mass spectrometer at the Massachusetts Institute of Technology.

Pb isotopic measurements were made in dynamic mode using four Faraday cup detectors and an axial, ion-counting Daly detector. An internal Daly-Faraday gain calibration was obtained by peak-switching the ^{205}Pb isotope peak into the axial position. U isotopes were measured as oxide ions in static mode on three Faraday cup detectors with an average $^{235}U^{16}O_2^+$ ion-beam intensity of 100 mV. Measured isotopic ratios were

corrected for mass-dependant isotope fractionation in the mass spectrometer, as well as for U and Pb contributions from the spike, laboratory blanks and the initial Pb in the sample. U-Pb isotopic dates and their associated uncertainties (Table 2) were calculated using the decay constants of Steiger and Jäger [19] and the error propagation algorithm of [31]. See Table 2 for further details, including fractionation, total procedural blanks, and complete isotopic data for each grain analyzed.

With the exception of u3, the isotopic composition of Pb in the grains we analyzed was highly radiogenic (Table 2), such that calculated U-Pb dates are not strongly dependent on our choice of a common Pb correction scheme. Moreover, using Pb isotopic compositions of HF-leached feldspars from other Himalayan leucogranites that display a relatively wide range of common Pb compositions [e.g. 6, 7, 32] produced insignificant changes in the plotting coordinates in concordia space of the 00KG20 uraninites. As a consequence, we did not attempt to measure common Pb for 00KG20 directly and relied instead on the Stacey and Kramers [33] model values.

RESULTS

After matrix and Y and Th interference corrections were applied, elemental concentrations of U, Th, Pb, Y, and O (in weight %) were re-normalized to sum to 100% and the elemental concentrations were recast in ppm (Table 1). In most cases, the sum total of U, Th, Pb, Y, and O was close to 100% by weight before re-normalization (Table 1) indicating that these species comprise the bulk composition of grain u5. The significant (i.e. ppm level) amounts of Th and Y are consistent with previous measurements of natural uraninite [34]. Generally, the 0-3% unaccounted for may be due to trace amounts of Nd, Ra, Ce, N, He, A, and/or OH^- commonly present in uraninite that

we did not measure [e.g. 34, 35]. Those analyses with anomalously low totals (e.g. ≤ 96%; italicized in Table 1) may also have been adversely affected by non-idealities (i.e. pits and roughness) on the polished grain surface (Figure 2c & d). Those points were excluded from the calculation of mean chemical dates.

Spatial Variations in U, Th, Pb, and Y Concentrations

The lack of contrast variations in the BSE image (Figure 2d) implies that no significant variations in mean atomic weight occur within grain u5. This preliminary observation belies textural and other chemical evidence for significant variability within the grain. For instance, the prominent, octahedrally-symmetric intra-grain boundary visible in the SE and BSE (Figure 2c & d, respectively) images strongly suggests concentric structural zonation and allows us to define a core and a rim which we interpret to be the result of episodic crystal growth.

Moreover, our point chemical data indicate that the rim and core of u5 have significantly different U, Th, and Y concentrations (Table 2). Superimposed on Figure 2c & d is a map of the twenty-four spots analyzed for the calculation of total U-Th-Pb chemical dates. Concentration profiles – plots of elemental concentration as a function of position outwards from the center of the crystal – display discontinuities that coincide exactly with the structural break between the core and rim (Figure 3). Average U concentration along Transects 1 and 2 is ca. 85% in the core compared to ca. 81% in the rim (Figure 3a). The core and rim are very well defined by the U distribution, and the chemical discontinuity between them is fairly sharp, occurring over a distance of ca. 25 μm. Conversely, Th concentration along Transect 1 rises from an average of ca. 2.7% in the core to ca. 6.3% in the rim, a profile that is the mirror image of that for U and equally

well defined (Figure 3b). Although Th concentrations are slightly different along Transect 2, averaging ca. 2.4% in the core vs. ca. 6.3% in the rim, the pattern is the same as that along Transect 1 (Figure 3b). Y concentration is closely correlated with Th concentration along both transects (Figure 3c). Average Y concentration in Transect 1 rises from ca. 0.35% in the core to ca. 0.87% in the rim, whereas along Transect 2, core Y concentration averages ca. 0.32%, which rises to ca. 0.89% in the rim. When contoured and superimposed on the SE image of grain u5, the elemental concentration data from Transects 1 and 2 match exactly the structural zonation of the crystal, exhibiting a high U-low Th-low Y core, and a low U-high Th-low Y rim (Figure 2e).

By contrast, Pb concentration (Table 2) along either transect does not display simple systematics. Along Transect 1, there is no discontinuity in Pb concentration at the structural break (Figure 3d). Instead, a group of five points within the core has an elevated average Pb concentration of ca. 0.26% compared to an average of ca. 0.21% along the rest of the transect. Along Transect 2, three points – the centermost point and two at the rim – have anomalously high Pb concentration, averaging ca. 0.23% compared to an average of ca. 0.21% along the rest of the transect. The contour plot of Pb concentration bears little resemblance to those for U, Th, and Y and does not conform to any morphologic features visible on the imaged surface of u5 (Figure 2e).

Electron Microprobe Chemical Dates

Table 2 summarizes the total U-Pb-Th chemical dates calculated with equation (1) and the electron microprobe data for each point along both transects through grain u5. Dates along Transect 1 vary substantially between 23.00 Ma and 17.34 Ma. Similarly, dates along Transect 2 vary between 20.28 Ma and 16.79 Ma. For every point analysis,

the propagated 2σ (95% confidence level) uncertainty is ca. 1.50 Ma.

A contour plot of the chemical dates along both transects does not conform to crystal morphology (Figure 2e), and when plotted as age profiles as a function of distance from the center of the crystal (Figure 3e & f), it is apparent that the chemical dates are closely correlated with Pb concentration and not with the distributions of U, Th, or Y (c.f. Figures 2e & 3). Chemical dates along Transect 1 are anomalously old for the same group of five points within the core of u5 that have elevated Pb concentrations (Figure 3e). Similarly, those points along Transect 2 that had high Pb concentrations are also anomalously old (Figure 3f). In either case, the distribution of chemical dates is not consistent with simple, concentric growth zonation of the crystal.

With the exception of the clusters of older points with anomalously high Pb concentrations, chemical dates are otherwise consistent from point to point along both transects (Figure 3g). We calculated separate mean chemical dates for each transect, as well as a mean chemical date considering all the point analyses. These averages excluded the older outlier points, as well as those with low totals (Table 1). Uncertainty in the average chemical dates is taken as two standard errors (2SE) of the mean. For Transect 1, the mean chemical date is 18.17 ± 0.52 Ma (Table 1; Figure 3e). The seven reliable dates included in the average are statistically indistinguishable, with a mean squared weighted deviation (MSWD) of 1.07, well within uncertainty of the ideal value of 1.0 [36]. The mean chemical date for the eight reliable dates along Transect 2 is 17.77 ± 0.59 Ma, although with a larger MSWD of 2.01 (Table 1; Figure 3f). Taken as a whole, these fifteen chemical dates have an average of 17.96 ± 0.40 Ma (MSWD = 1.22) (Table 1; Figure 3g) that we regard as a reliable estimate of the age of grain u5. By

comparison, the mean age of the total of seven outlier points (excluding anomalously old points and those with low totals) along both transects is 21.12 ± 0.97 Ma, with an unacceptably high MSWD of 3.47.

ID-TIMS Dates

Monazite grain m1 plots nearly concordantly (Figure 4a & b) with a $^{207}Pb/^{235}U$ date of 18.28 ± 0.10 Ma (Table 2). Although all seven uraninite grains yielded very precise ID-TIMS dates, all were substantially normally discordant when plotted on a concordia diagram (Figure 4a), and their significance with respect to the crystallization age of 00KG20 is not obvious. Individual $^{207}Pb/^{235}U$ dates range between 17.139 Ma and 16.436 Ma (Table 2), and the seven analyses define a linear array in $^{206}Pb/^{238}U$ vs. $^{207}Pb/^{235}U$ space that is essentially parallel to concordia (Figure 4a). Given such a linear array of data, one way to estimate a crystallization age is to calculate the upper intercept of the chord defined by the array with concordia. A linear regression of this data yields a statistically unreliable upper intercept of $19.22^{+95.21}_{-1.55}$ Ma (MSWD = 16.5) (Figure 4a).

It is appropriate, however, to consider the effect of ^{230}Th deficiency within extremely U enriched phases such as uraninite. Deficiency in initial ^{230}Th will, in turn, cause deficiency in ^{206}Pb, resulting in anomalously low $^{206}Pb/^{238}U$ dates and normally discordant data points. One approach is to apply the correction described by Parrish [11]:

$$\left(\frac{^{206}Pb}{^{238}U}\right)_{corrected} = \left(\frac{^{206}Pb}{^{238}U}\right)_{measured} \left(\frac{\left(\frac{Th}{U}\right)_{mineral}}{\left(\frac{Th}{U}\right)_{magma}} - 1\right)\left(\frac{\lambda_{238}}{\lambda_{230}}\right) \quad (2),$$

where the "corrected" subscript refers to the ^{230}Th deficiency corrected value, the "measured" subscript indicates the value from the ID-TIMS analyses, the "mineral" subscript indicates the Th/U ratio of the uraninite grain, the "magma" subscript indicates the Th/U ratio of the source magma, and λ_{238} and λ_{230} are the decay constants (in yr^{-1}) for ^{238}U, and ^{230}Th, respectively [19]. For this correction, we must assume a Th/U ratio for the parent magma. Although that specific data is not available for the Mugu granite, we use the Th/U ratio determined for the parent magma of a similar intrusion, the Manaslu pluton [0.689; 37].

The effect of the correction is to shift the ^{206}Pb/^{238}U of each analysis by ca. 1.5 x 10^{-5}, moving the data points upward along the ^{206}Pb/^{238}U axis towards concordia (Figure 4b). Thus corrected a linear regression of these data using a modified version of the algorithm derived by York [38] – specifically Model 2 of Ludwig [39] – yields an upper concordia intercept corresponding to a date of $17.63^{+108.72}_{-0.63}$ Ma (Figure 4b), although it is still not a statistically significant linear correlation (MSWD = 19.8). Since the upper intercept is dependent on an assumption of a magmatic Th/U, a value for which we have no specific constraint, and because the quality of both linear regressions is poor, we suggest that the grain with the oldest ^{207}Pb/^{235}U date (u4b; 17.139 ± 0.011 Ma [2σ]; Table 2) gives the best minimum constraint on the crystallization age of uraninite in 00KG20.

DISCUSSION

Comparison of Chemical Dating and ID-TIMS Results

Table 3 summarizes the U-Th-Pb geochronologic constraints resulting from our analysis of monazite and uraninite from sample 00KG20. Since it is the oldest date

obtained from the sample, we take the 18.28 Ma $^{207}Pb/^{235}U$ date from monazite grain m1 as our best estimate of a minimum crystallization age for 00KG20. That this age is within uncertainty of the upper intercept of the uraninite ID-TIMS data (17.63 Ma) supports this conclusion if we interpret the uraninite data to reflect Pb loss.

Within uncertainty, all three mean chemical dates agree with each other and with the monazite (m1) $^{207}Pb/^{235}U$ ID-TIMS date, falling in the range between 18.69 Ma and 17.18 Ma (Table 3). Within uncertainty, the mean chemical dates also agree with the 17.63 Ma upper intercept resulting from linear regression of the ^{230}Th deficiency corrected uraninite ID-TIMS data, although the uncertainties in question are rather large (Table 3). The similarity between both of these ID-TIMS results and the mean chemical dates, despite the large uncertainties, is encouraging because it shows that the chemical dating technique may be an expedient method for reconnaissance geochronology of leucogranites. The very precise 17.139 Ma $^{207}Pb/^{235}U$ ID-TIMS date (u4b) we interpret as a minimum constraint on uraninite crystallization, falls just outside of the range of the other constraints (Table 3).

Because we do not know the specific Th/U of the magma from which the Mugu granite crystallized, the absolute significance of the uraninite ID-TIMS upper intercept date is uncertain. However, the similarity it has to the mean chemical dates may suggest that the Th/U ratio we use is a reasonable estimate. In any case, the simplest interpretation of the ID-TIMS results is that the linear arrays in Figure 4 represent substantial, but variable, Pb loss subsequent to crystallization of 00KG20 (m1: 18.28 Ma; Table 3) and prior to the $^{207}Pb/^{235}U$ date of the oldest uraninite grain (u4b: 17.139 Ma; Tables 3). Moreover, the fact that individual fragments of the same crystal (u4a-d)

neither yield identical dates (Table 2) nor plot identically on the concordia diagram (Figure 4) suggests that Pb loss was complex and occurred on both inter- and intra-grain scales, a hypothesis we explore in more detail below.

Chemical Zonation and Episodic Growth of Uraninite

Strictly speaking, uraninite, UO_2, refers to the U-rich end-member of a solid solution series in which U and Th substitute for one another, with thoraninite, ThO_2, as the Th-rich end-member. The chemical difference between the core and rim of grain u5 suggests a change in magmatic conditions during uraninite growth that signaled an increase in thoraninite crystallization in the rim. At the same time, the marked increase in Y concentration in the rim suggests that the magma from which grain u5 crystallized became more enriched in REE (rare earth elements) as time progressed. However, in both the cases of U and Th as well as REE, the fact that the concentration profiles (Figure 3a-c) are abrupt step-functions rather than more gradual ones suggests that there may have been a hiatus in uraninite growth during which the changes in magmatic chemistry occurred. However, the lack of any similar pattern among the chemical dates within grain u5 (e.g. Figures 2e & 3e-g) also suggests that any such hiatus was not prolonged, lasting no more than ca. 1.5 Ma, the uncertainty in our chemical dates (Table 1). That the entire growth history of the uraninite in sample 00KG20 was a short one is also hinted at by the peculiar mineralogy of some of the inclusions within grain u5. The preservation of inclusions of diopside and fayalite, both expected to dissolve quickly in a leucogranitic melt, suggests that encapsulation of the inclusions was a rapid process and that uraninite was an early solidus phase in the melt that crystallized as the 00KG20 dike.

U, Th, Pb and Y Diffusion in Uraninite

The hypothesis that Pb mobility in uraninite is an important contributor to the U-Th-Pb systematics of grain u5 is supported by the spatial patterns of elemental concentrations we measured with the electron microprobe. We note that the spatial distribution of Pb is completely unlike that of U, Th, and Y and that it does not match the grain morphology (e.g Figure 2e). Moreover, the pattern of chemical dates in grain u5 – which mirrors that of Pb concentration – is not compatible with the simple concentric growth zonation suggested by grain morphology and the distributions of U, Th, and Y (e.g. Figure 2e). This is especially true along Transect 2 where the oldest chemical dates are found in the rim of u5 (Figure 3f). These observations suggest to us that the process responsible for the distribution of Pb may be different than that responsible for the distribution of U, Th, and Y. In addition, we can infer that the measured distribution of Pb likely came about at some point after crystallization of the grain. Quantitative examination of the distributions of U, Th, and Y can give us a framework for understanding the processes at work.

Although the structural interface between the chemically distinct core and rim of grain u5 marks relatively sharp discontinuities in U, Th, and Y, the geometry of the concentration profiles across the boundary are suggestive of diffusive transfer patterns that developed during post-crystallization cooling (Figure 3a-c). We model this process using the equations for an infinite composite medium for the case of two infinite halfspaces, each with diffusivity, D_n (in $cm^2\ s^{-1}$) at a given temperature, in contact along an interface at $x = 0$, [40]:

$$\frac{C_1}{C_0} = \frac{1}{2}\left[1 + erf\left(\frac{x}{2\sqrt{D_n t}}\right)\right], \qquad \text{for } x > 0 \qquad (3a)$$

$$\frac{c_2}{c_0} = \frac{1}{2}\left[erfc\left(\frac{|x|}{2\sqrt{D_n t}}\right)\right], \qquad \text{for } x < 0 \qquad (3b),$$

where x is the spatial coordinate (in cm), t is time (in s); c_1 is the concentration in the region $x > 0$ (in ppm), c_2 is the concentration in the region $x < 0$ (in ppm), and c_0 is the initial concentration in the region $x > 0$ (in ppm). It is assumed that the initial concentration in the region $x < 0$ is zero, and that equilibrium is attained when the concentrations in both regions are equal (e.g. $\frac{c_1}{c_2} = 1$, for all x when $t = t_{equilibrium}$).

To fit equations (3ab) to the measured U, Th, and Y concentration profiles, we linearize equations (3ab) by inverting through the error function:

$$\frac{x}{2\sqrt{D_n t}} = erf^{-1}\left[2\frac{c_1}{c_0} - 1\right], \qquad \text{for } x > 0 \qquad (4a)$$

$$\frac{|x|}{2\sqrt{D_n t}} = erf^{-1}\left[1 - 2\frac{c_1}{c_0}\right], \qquad \text{for } x < 0 \qquad (4b).$$

For U, Th, and Y, we take c_0 as the maximum concentration along the profile and we plot $erf^{-1}\left[2\frac{c_1}{c_0} - 1\right]$ as a function of x. The slope of the best-fit line through the data is then proportional to $\frac{1}{2\sqrt{D_n t}}$, while the x intercept is equal to x'_b. Unfortunately, along Transect 2 there are too few points in the transitional section of the concentration profiles to yield good fits with this method, so we focus on the results from Transect 1 (Figure 5). The U and Th concentration profiles in Transect 1 yield similar $D_n t$ values of 2.76×10^{-6} cm^2 and 2.99×10^{-6} cm^2, respectively. For Y, $D_n t$ is 6.19×10^{-6} cm^2, about a factor of 2 higher. Furthermore, presuming that all Pb in the sample is radiogenic, the relative homogeneity of its concentration across the core-rim interface in grain u5 (Figure 3d) –

despite a significant difference in U/Th ratio across the interface (Table 2) – suggests that Pb is substantially more mobile in the uraninite structure than U, Th, or Y. From these results we can make a general statement about the relative diffusivity of Pb, U, Th, and Y in grain u5 and infer that:

$$D_{nPb} > D_{nU} = D_{nTh} = \frac{1}{2} D_{nY} \quad (5),$$

assuming that the profiles are diffusive and were established under uniform cooling conditions over the same length of time

Few previous workers have studied UO_2, although early studies did arrive at estimates for Pb diffusivity in uraninite as well as models for the structure of uraninite and its effect on diffusion through the material. Yershov [41] advocated a complex structure for natural uraninite wherein Pb resides in either "stable" or "unstable" sites. This structure is produced during self-oxidation of uraninite [U^{+4} to U^{+6}; 42, 43], which triggers exsolution of tabular PbO domains along unit-cell boundaries. Whereas Yershov [41] estimated the diffusivity of Pb in stable zones at 700 °C to be ca 10^{-17} cm^2 s^{-1}, he suggested that the unstable zones could serve as faster diffusion pathways with diffusivities of ca. 10^{-13} cm^2 s^{-1}, at least 1000 times greater than the rest of the crystal. Based on these estimates, the ca. 100 μm scale redistribution of Pb along fast pathways within grain u5 could have been produced within ca. 0.3 Ma at a temperature of 700 °C, a reasonable estimate of the magmatic temperature of the Mugu granite. Furthermore, based on equation (5), we can estimate that the diffusivity of U, Th, and Y should be no greater than 10^{-17} cm^2 s^{-1} at 700 °C.

Estimates of diffusivity of U in natural uraninite do not exist, although some estimates exist for U diffusivity in artificial, metallic UO_2 used as a fuel in nuclear

reactors. Most recently, Sabioni *et al.* [44] reported Arrhenius parameters for U in near-optimum density, synthetic UO_2:

$$D_n = D_0 \exp\left(\frac{E_a}{RT}\right)$$
$$D_0\left(cm^2\ s^{-1}\right) = 8.54 \times 10^{-7} \quad (6),$$
$$E_a\left(kJmol^{-1}\right) = 425.54$$

where D_n is the diffusivity (in $cm^2\ s^{-1}$) at temperature T (in K), D_0 is the diffusivity at infinite temperature, E_a is the activation energy, and R is the gas constant (8.31451 J mol-*1* K-*1*). If we use equation (6) in conjunction with our measured value of $D_n t$ for U in uraninite u5 (2.76×10^{-6} $cm^2\ s^{-1}$), we can make an estimate of the time required to develop the U concentration profiles we observe given a reasonable range of temperatures, or *vice versa*. We find that for any reasonable choice of temperature, the time required is geologically unrealistic (Table 4). Similarly, for any geologically reasonable period of time, the required temperature is impossibly high (Table 4).

There are several possible explanations for this. The most likely is that the Arrhenius parameters of Sabioni *et al.* [44] are not applicable to natural uraninite, although the possibility exists that the concentration profiles we observe in grain u5 are not due to diffusion at all and may reflect another process. However, in addition to the parameters in equation (6), Sabioni *et al.* [44] reviewed several previous estimates of the Arrhenius parameters for U in UO_2. All of these have substantially larger D_0. For instance Yajima *et al.* [45] suggests that $D_0 = 1 \times 10^{-4}$ $cm^2\ s^{-1}$ and $E_a = 290$ kJ mol^{-1}. Using these values instead of those of Sabioni *et al.* [44] results in more realistic temperatures and times (Table 4). In addition, we note that D_n at 700 °C (ca. 10^{-20} $cm^2\ s^{-1}$) using the Arrhenius parameters of Yajima *et al.* [45] is consistent with our estimate ($< 10^{-17}$ $cm^2\ s^{-1}$)

based on the relative diffusivity of U and Pb (equation [6]) and the estimated fast pathway diffusivity of Pb at 700 °C [41].

Estimating the Degree of Pb Loss

We have shown that within the large uncertainties that inherent to the technique that the resulting chemical dates are consistent with ID-TIMS dates. In detail, however, it is clear that Pb loss will affect both ID-TIMS and chemical dates, making the dates we measure less than the actual age of the grain. The question remains: to what extent has Pb loss from uraninite affected the dates we measure? Our electron microprobe study of grain u5 allows us to make an estimate of the degree of Pb loss.

The relationship between chemical age and Pb concentration as described by equation (1) – assuming that the concentrations of U and Th are equal to the mean concentrations from grain u5 (U: ca. 83.72%, Th: ca. 3.65%; Table 1) – is a linear one with a slope of 0.084 Ma per ppm. If we assume that the ca. 17.63 Ma ID-TIMS upper intercept date for uraninites u1-u3 & u4a-d is indicative of the true crystallization age of uraninite in 00KG20, Pb loss ranges between ca. 58 ppm (for u4b) and 142 ppm (for u4d). Assuming that the mean concentration of Pb (ca. 0.22%; Table 1) in grain u5 is applicable to the other uraninite grains in 00KG20, this translates into Pb loss of between ca. 2.5% (for u4b) and ca. 5.9% (for u4d). These estimates are based on the discrepancies between the individual uraninite $^{207}Pb/^{235}U$ dates (Table 1) and the uraninite upper intercept date (Figure 4b; Table 3). According to this scheme, grain u5 has essentially no Pb loss since its mean chemical date is within uncertainty (actually older than) the upper intercept age (Table 3). Alternatively, if we use the ca. 18.28 Ma ID-TIMS date from monazite m1 (Table 3) as the true uraninite crystallization age, we

surmise between ca. 135 ppm, or ca. 5.7%, (u4b) and ca. 219 ppm, or ca. 8.9%, (u4d) Pb loss for uraninites u1-u3 & u4a-d. According to this scheme grain u5 has experienced ca. 38 ppm (ca 1.7%) of Pb loss.

CONCLUSION

Comparison between the results of the electron microprobe work and ID-TIMS dating of uraninite from the same sample of Mugu leucogranite suggests that electron microprobe chemical dating of uraninite may be a useful reconnaissance tool for the geochronology of rocks containing this mineral. The calculated mean chemical dates are within uncertainty of other estimates for the crystallization age of the granite as determined by more precise ID-TIMS measurements. Nevertheless, gaining the high spatial resolution of electron microprobe geochronology comes at a price: losing some analytical precision. ID-TIMS U-Pb geochronology of uraninite may, under the best circumstances, yield results with a precision that is up to two orders of magnitude greater than that for electron microprobe chemical dating of uraninite. However, we have shown that uraninite as young as ca. 18.3 Ma can be successfully dated by chemical means with an uncertainty of less than a million years, which is adequate to address many tectonic problems.

Examination of chemical data from uraninite u5 reveals spatial patterns in U, Th, and Y concentrations indicative of diffusion across the structural interface between a chemically distinct core and rim. By contrast, Pb concentration does not display any such diffusive profile. From the form of the concentration profiles, we infer that the diffusivity of Pb is much higher than those of U, Th, or Y in the uraninite family of minerals. Quantitative modeling of the U, Th, and Y concentration profiles, combined

with previous estimates for the Arrhenius parameters governing U diffusion in synthetic UO_2 and the diffusivity of Pb in uraninite, suggest that the diffusivity of U, Th, and Y in uraninite is less than 10^{-7} cm^2 s^{-1} at ca. 700 °C. Pb diffusivity is substantially higher and suggests the possibility that mobility and loss of Pb has affected ID-TIMS analyses of other grains from sample 00KG20. We estimate the amount of Pb loss to be as much as 8.9%.

Bearing the complexities in mind, we advocate the integrated use of electron microprobe and ID-TIMS methods whenever feasible. Electron microprobe chemical dating can be applied quickly and cheaply to uraninites from numerous samples, and the results may be used to select appropriate samples for higher precision ID-TIMS work. In addition, the high spatial resolution of the electron microprobe may help with the interpretation of ID-TIMS results for the many leucogranite samples that contain multiple generations of accessory minerals. In older samples, electron microprobe chemical dating of accessory minerals such as monazite may add an additional dimension to such research. Finally, as we have shown, detailed electron microprobe work can also illuminate situations wherein Pb loss or mobility has affected ID-TIMS analyses.

ACKNOWLEDGEMENTS

This research was supported by a grant from the U. S. National Science Foundation (NSF) awarded to KVH, J. P. Grotzinger, and Kelin X Whipple (EAR-9706216) and an NSF graduate fellowship awarded to JMH. JMH thanks the Frank and Eva B. Buck Foundation for their continuing financial support.

REFERENCES CITED

1 K.V. Hodges, Tectonics of the Himalaya and southern Tibet from two perspectives, Geological Society of America Bulletin 112(3), 324-350, 2000.

2 U. Schärer, The effect of initial ^{230}Th disequilibrium on young U-Pb ages: the Makalu case, Himalaya, Earth and Planetary Science Letters 67, 191-204, 1984.

3 S.R. Noble and M.P. Searle, Age of crustal melting and leucogranite formation from U-Pb zircon and monazite dating in the western Himalaya, Zanskar, India, Geology 23(12), 1135-1138, 1995.

4 M.P. Searle, R.R. Parrish, K.V. Hodges, A. Hurford, M.W. Ayers and M.J. Whitehouse, Shisha Pangma leucogranite, South Tibetan Himalaya: Field relations, geochemistry, age, origin, and emplacement, Journal of Geology 105, 295-317, 1997.

5 M.E. Coleman, U-Pb constraints on Oligocene-Miocene deformation and anatexis, Marsyandi Valley, central Nepalese Himalaya, American Journal of Science 298, 553-571, 1998.

6 K. Hodges, S. Bowring, K. Davidek, D. Hawkins and M. Krol, Evidence for rapid displacement on Himalayan normal faults and the importance of tectonic denudation in the evolution of mountain ranges, Geology 26, 483-486, 1998.

7 K.M. Viskupic and K.V. Hodges, Monazite-xenotime thermochronology: methodology and an example from the Nepalese Himalaya, Contributions to Mineralogy and Petrology 141, 233-247, 2001.

8 T.M. Harrison, K.D. McKeegan and P. LeFort, Detection of inherited monazite in the Manaslu leucogranite by ^{208}Pb/^{232}Th ion microprobe dating: Crystallization age and tectonic implications, Earth and Planetary Science Letters 133, 271-282, 1995.

9 T.M. Harrison, F.J. Ryerson, K.D. McKeegan, P. Le Fort and A. Yin, Th-Pb monazite ages of Himalayan metamorphic and leucogranitic rocks: Constraints on the timing of inverted metamorphism and slip on the MCT and STD, in: 11th Himalaya-Karakoram-Tibet Workshop Abstracts, A.M. Macfarlane, R.B. Sorkhabi and J. Quade, eds., pp. 58-59, 1996.

10 T.M. Harrison, O.M. Lovera and M. Grove, New insights into the origin of two contrasting Himalayan granite belts, Geology 25, 899-902, 1997.

11 R. Parrish, U-Pb dating of monazite and its application to geological problems, Canadian Journal of Earth Sciences 27, 1431-1450, 1990.

12 K.V. Hodges, R. Parrish, T. Housh, D. Lux, B.C. Burchfiel, L. Royden and Z. Chen, Simultaneous Miocene extension and shortening in the Himalayan orogen, Science 258, 1466-1470, 1992.

13 J.-M. Montel, S. Foret, M. Veschambre, C. Nicollet and A. Provost, Electron microprobe dating of monazite, Chemical Geology 131, 37-53, 1996.

14 M.L. Williams, M.J. Jercinovic and M.P. Terry, Age mapping and dating of monazite on the electron microprobe: deconvoluting multistage tectonic histories, Geology 27(11), 1023-1026, 1999.

15 J.F.W. Bowles, Age dating of individual grains of uraninite in rocks from electron microprobe analyses, Chemical Geology 83, 47-53, 1990.

16 H.J. Förster, The chemical composition of uraninite in Variscan granites of the Erzgebirge, Germany, Mineral. Mag. 63(2), 239-252, 1999.
17 T.G. Kotzer and T.K. Kyser, O, U, and Pb isotopic and chemical variations in uraninite: implications for determining the temporal and fluid history of ancient terrains, American Mineralogist 78, 1262-1274, 1993.
18 U. Kempe, Precise electron microprobe age determination in altered uraninite: consequences on the intrusion age and the metallogenic significance of the Kirchberg granite (Erzgebirge, Germany), Contributions to Mineralogy and Petrology 145, 107-118, 2003.
19 R.H. Steiger and E. Jäger, Subcommission on geochronology: convention on the use of decay constants in geo- and cosmochronology, Earth and Planetary Science Letters 36, 359-362, 1977.
20 M.P. Terry, P. Robinson, M.A. Hamilton and M.J. Jercinovic, Monazite geochronology of UHP and HP metamorphism, deformation, and exhumation, Nordoyane, Western Gneiss region, Norway, American Mineralogist 85(11-12), 1651-1664, 2000.
21 A. Cocherie, O. Legendre, J.J. Peucat and A.N. Kouamelan, Geochronology of polygenetic monazites constrained by in situ electron microprobe Th-U total lead determination - implications for lead behavior in monazite, Geochimica et Cosmochimica Acta 62, 2475-2497, 1998.
22 P. Le Fort and C. France-Lanord, Granites from Mustang and surrounding regions, central Nepal, Journal of the Nepal Geological Society 10, 79-81, 1995.
23 J.M. Hurtado, Jr., Tectonic Evolution of the Thakkhola Graben and Dhaualgiri Himalaya, Central Nepal, Ph.D., Massachusetts Institute of Technology, 2002.
24 J.T. Armstrong, A package of correction programs for the quantitative electron microbeam x-ray analysis of thick polished materials, thin-films, and particles, Microbeam Analysis 4, 177-200, 1995.
25 P. Duncumb and S.J.B. Reed, Quantitative Electron Probe Microanalysis, in: National Bureau of Standards Special Publication 298, K.F.J. Heinrich, ed., pp. 133, 1968.
26 K.F.J. Heinrich, National Bureau of Standards, Technical Note 521, 1969.
27 S.J.B. Reed, Characteristic fluorescence correction in electron-probe microanalysis, British Journal of Applied Physics 16(913-926), 1965.
28 G.M. Anderson, Error propagation by the Monte Carlo method in geochemical calculations, Geochimica et Cosmochimica Acta 40, 1533-1538, 1976.
29 A.P. White, Extensional Evolution of the Central East Greenland Caledonides, Ph.D., Massachusetts Institute of Technology, 2001.
30 T.E. Krogh, A low-contamination method for hydrothermal decomposition of zircon and extraction of U and Pb for isotopic age determinations, Geochimica et Cosmochimica Acta 37(3), 485-494, 1973.
31 K.R. Ludwig, Calculation of uncertainties of U-Pb isotope data, Earth and Planetary Science Letters 46, 212-220, 1980.

32 C. Gariépy, C.J. Allègre and R.-H. Xu, The Pb-isotope geochemistry of granitoids from the Himalaya-Tibet collision zone: implications for crustal evolution, Earth and Planetary Science Letters 74, 220-234, 1985.
33 J.S. Stacey and J.D. Kramers, Approximation of terrestrial isotope evolution by a two-stage model, Earth and Planetary Science Letters 26, 207-221, 1975.
34 K.G. Snetsinger and G. Polkowski, Rare accessory uraninite in a Sierran granite, American Mineralogist 62, 587-588, 1977.
35 C. Klein and C.S.J. Hurlbut, Manual of Mineralogy (after James D. Dana), 681 pp., John Wiley & Sons, Inc., New York, 1993.
36 I. Wendt and C. Carl, The statistical distribution of the mean squared weighted deviation, Chemical Geology 86, 275-285, 1991.
37 P. Le Fort, M. Cuney, C. Deniel, C. France-Lanord, S.M.F. Sheppard, B.N. Upreti and P. Vidal, Crustal generation of Himalayan leucogranites, Tectonophysics 134, 39-57, 1987.
38 D. York, Least-squares fitting of a straight line with correlated errors, Earth Planet. Sci. Lett. 5, 320-324, 1969.
39 K.R. Ludwig, Isoplot; a plotting and regression program for radiogenic-isotope data; version 2.53, U.S. Geological Survey Open File Report 91-0445, 39p., 1991.
40 J. Crank, The Mathematics of Diffusion, 414 pp., Oxford University Press, London, 1975.
41 V.M. Yershov, A method of examining the diffusion parameters of lead in uranium minerals, Geochemistry International 11, 1099-1101, 1974.
42 H.V. Ellsworth, Pan. Am. Geol. 42, 273, 1924.
43 R.M. Berman, The role of lead and excess oxygen in uraninite, American Mineralogist 42(11 & 12), 705-729, 1957.
44 A.C.S. Sabioni, W.B. Ferraz and F. Millot, First study of uranium self-diffusion in UO2 by SIMS, Journal of Nuclear Materials 257, 180-184, 1998.
45 S. Yajima, H. Furuya and T. Hiroi, Journal of Nuclear Materials, 162, 1966.
46 M. Colchen, P. LeFort and A. Pêcher, Rechereches Géologiques dans l'Himalaya du Népal: Annapurna - Manaslu - Ganesh Himal (Notice de la carte géologique au 1/200000), 136 pp., Centre National de la Recherche Scientifique, Paris, 1986.

FIGURE CAPTIONS

Figure 1.

Map showing the location of the Thakkhola graben and Upper Mustang Massif (UMM) (inset) and generalized geology of the region.

Figure 2.

a. Photograph of the Mugu granite dike from which sample 00KG20 was taken. View to the southwest. Field book for scale is 12 cm by 19 cm. The country rock is deformed Silurian to Devonian calcic pelitic schist of the Tibetan Sedimentary sequence [22, 46] metamorphosed to lower-amphibolite facies. Compositional layering in the country rock strikes east and dips moderately south, whereas the dike strikes north and dips steeply west. The dike is undeformed and cuts across older, deformed Mugu granite dikes (not shown) and the deformational fabrics in the country rock.

b. Photomicrographs of uraninite crystals from 00KG20. Grains u1-u4a-d were used for ID-TIMS analysis, and grain u5 (not shown, but similar in size and appearance to the unbroken u4) was used for electron microprobe work. Note the specular patina on the uraninite grains (e.g. light colored patches on u1, u3, and u4) indicative of pervasive inclusions. Images taken with a digital camera mounted to a binocular microscope. The grains, immersed in an ethanol bath, were imaged with a digital camera under reflected light at a magnification of 6.3x (see scale bar).

c. Secondary electron (SE) image of grain u5. Note the abundant pits and voids due to excavated inclusions. Some form a concentric band parallel to the crystal faces. Labeled circles denote locations of spot analyses in Transect 1. Crosses denote spot

analyses in Transect 2. Spot sizes (ca. 1 μm) are smaller than the diameter of the symbols.

d. Back-scattered electron (BSE) image of grain u5. Note the lack of any obvious variation in grayscale within the grain, suggesting a lack of intra-grain gradients in chemical composition. Labeled circles denote locations of spot analyses in Transect 1. Crosses denote spot analyses in Transect 2. Spot sizes (ca. 1 μm) are smaller than the diameter of the symbols.

e. Contour plots of U, Th, Y, Pb, and chemical age superimposed on the SE image for u5. Contours of U, Th, and Y concentrations conform closely to the structural zonation visible in the crystal. Contours of Pb and chemical age do not conform to crystal morphology. Labeled circles and crosses denote locations of spot analyses. Spot sizes (ca. 1 μm) are smaller than the diameter of the symbols. Plain SE image in lower right corner is for reference.

Figure 3.

Along-transect profiles of elemental concentrations and chemical dates. Units along the x-axis are in μm from the center of the grain. The center of the grain (x = 0 μm) is taken as the position of the first point in the transect. The core region of the grain is that closest to the center, and the rim is on the periphery. Concentration is in ppm. Dates are in Ma. Error bars denote the 2σ (95%) confidence intervals.

a. U concentration profile along Transect 1 and 2.

b. Th concentration profile along Transect 1 and 2.

c. Y concentration profile along Transect 1 and 2.

d. Pb concentration profile along Transect 1 and 2.

e. Chemical age profile along Transect 1

f. Chemical age profile along Transect 2.

g. Plot of combined chemical dates for both transects.

Figure 4.

Concordia diagrams for sample 00KG20. Curves with numbered tic marks represent concordia with labels in units of Ma. Data points include error ellipses representing 2□ (95%) analytical uncertainties. Data points are labeled by grain identifier (m = monazite; u = uraninite).

a. Uraninite analyses u1-u4a-d and monazite m1. Uraninite data have not been corrected for ^{230}Th deficiency [11]. Note that the uraninite analyses form a linear array essentially parallel to Concordia. A York [38] regression – specifically Model 2 of Ludwig [39] – through the uncorrected uraninite analyses yields an upper concordia intercept corresponding to a date of $19.22^{+95.21}_{\square 1.55}$ Ma (MSWD = 16.5).

b. Uraninite analyses u1-u4a-d and monazite m1. Uraninite data have been corrected for ^{230}Th deficiency [11]. Note that the correction moves the data points upward toward concordia slightly. A York [38] regression – specifically Model 2 of Ludwig [39] – through the corrected uraninite analyses yields an upper concordia intercept corresponding to a date of $17.63^{+108.72}_{\square 0.63}$ Ma (MSWD = 19.8).

Figure 5.

Inversion of concentration profiles through the inverse error function using equations (4ab). Diamonds are point analyses. Solid line is least squares linear fit through the data (equation and R^2 fit criterion given). The slope of the best-fit line is proportional to the quantity $D_n t$.

a. Transect 1 uranium.

b. Transect 1 thorium.

c. Transect 1 yttrium.

TABLE 1. ELECTRON MICROPROBE POINT DATA AND RESULTS FOR 00KG20 u5

Point†	X§ (mm)	U# (ppm)	±	2σ# (ppm)	Th# (ppm)	±	2σ# (ppm)	Pb# (ppm)	±	2σ# (ppm)	Y# (ppm)	±	2σ# (ppm)	O# (ppm)	Total†† (wt. %)	Date§§ (Ma)	±	2σ§§ (Ma)
Transect 1																		
1	0.0	851402.35	±	1907.14	23949.01	±	187.28	2197.86	±	166.77	3536.97	±	243.77	118918.92	98	**18.32**	**±**	**1.43**
2	8.9	851337.34	±	1941.05	24113.62	±	187.60	2274.52	±	169.00	3440.80	±	240.99	118909.39	*96*	*18.96*	±	*1.45*
3	15.0	852592.90	±	1909.81	22853.21	±	184.65	2132.50	±	166.59	3486.12	±	240.68	118926.09	98	**17.76**	**±**	**1.43**
4	24.0	850194.55	±	1921.44	24997.95	±	189.98	2491.30	±	172.10	3457.92	±	248.35	118881.83	98	20.78	±	1.48
5	35.4	849428.76	±	1987.66	26083.21	±	197.71	2731.19	±	178.62	3027.59	±	242.51	118775.60	*93*	*22.79*	±	*1.54*
6	47.5	847579.39	±	1932.48	27475.27	±	197.82	2382.09	±	173.80	3613.74	±	250.29	118896.41	*96*	*19.91*	±	*1.50*
7	51.5	839720.54	±	1914.56	34624.47	±	211.21	2514.13	±	170.01	4094.32	±	246.23	118976.68	97	21.15	±	1.48
8	54.9	848176.87	±	1950.81	26797.99	±	196.70	2753.56	±	176.12	3397.95	±	248.59	118818.11	*95*	*23.00*	±	*1.52*
9	62.9	840221.77	±	1898.90	34879.03	±	209.27	2061.49	±	165.08	3834.68	±	242.12	118951.61	99	**17.34**	**±**	**1.43**
10	77.1	826913.25	±	1885.36	46081.54	±	233.17	2069.07	±	164.95	5771.94	±	264.24	119239.81	98	**17.60**	**±**	**1.45**
11	83.0	814998.48	±	1874.50	56269.61	±	250.96	2225.48	±	164.51	7139.97	±	278.32	119421.11	99	**19.13**	**±**	**1.46**
12	94.2	806348.88	±	1870.73	62975.14	±	264.50	2082.39	±	165.01	8918.22	±	293.77	119683.58	97	**18.04**	**±**	**1.47**
13	103.9	806932.26	±	1904.36	62665.12	±	268.21	2019.44	±	167.05	8688.58	±	299.06	119623.80	*95*	*17.49*	±	*1.49*
14	115.9	806055.73	±	1853.93	63575.09	±	261.93	2193.94	±	166.39	8543.41	±	292.01	119605.67	99	**19.01**	**±**	**1.49**
														Transect 1 mean ± 2SE ##		18.17	±	0.52
Transect 2																		
1	0.0	851264.86	±	1906.83	24201.97	±	187.32	2269.63	±	168.09	3339.43	±	244.11	118866.20	98	**18.91**	**±**	**1.45**
2	8.9	851658.82	±	1890.68	23926.03	±	185.19	2040.69	±	165.50	3479.00	±	241.30	118873.41	100	**17.00**	**±**	**1.42**
3	18.4	851480.18	±	1907.32	24295.03	±	186.10	2157.55	±	167.56	3207.23	±	239.19	118815.86	100	**17.98**	**±**	**1.44**
4	26.2	852249.70	±	1909.04	23360.36	±	184.08	2199.03	±	166.55	3315.77	±	240.33	118869.07	99	**18.31**	**±**	**1.43**
5	42.4	852562.81	±	1892.69	23197.99	±	183.73	2138.69	±	166.18	3235.18	±	240.83	118894.47	100	**17.81**	**±**	**1.43**
6	47.4	852841.48	±	1893.31	23257.23	±	182.34	2016.95	±	164.87	3115.65	±	231.56	118843.47	100	**16.79**	**±**	**1.41**
7	60.8	850680.10	±	1905.52	24764.74	±	187.72	2013.10	±	166.44	3650.38	±	243.41	118891.69	99	**16.79**	**±**	**1.43**
8	73.2	826923.08	±	1901.92	45968.74	±	233.52	2383.79	±	169.82	5525.50	±	264.89	119189.63	97	20.28	±	1.49
9	80.8	806150.69	±	1870.27	63249.62	±	264.38	2144.54	±	165.64	8827.27	±	294.83	119630.96	98	**18.58**	**±**	**1.48**
10	89.5	805729.90	±	1853.18	63373.15	±	262.36	2302.09	±	166.44	8943.11	±	293.87	119659.85	99	19.95	±	1.49
														Transect 2 mean ± 2SE ##		17.77	±	0.59
														All points mean ± 2SE ##		17.96	±	0.40

Notes :

† See Fig. 2 for maps of the points superimposed on the back-scattered and secondary electron images. For Transect 1, Point 1 is near the center of the grain and Point 14 is at the edge. Similarly, for Transect 2, Point 1 is near the center and Point 10 is at the edge.

§ Radial distance outward from the center of the grain. The "center" is taken to be the position of the innermost point analysis. Note that Point 1 for Transect 1 is not in the same place as Point 1 for Transect 2, although both are in the approximate center of the grain (Fig. 2). For Transect 1, the structural break between core and rim is between Points 9 and 10. For Transect 2 the structural break between core and rim is between Points 7 and 8.

Concentrations determined by wavelength dispersive spectrometry (WDS) using PET diffracting crystals calibrated with UO_2, ThO_2, $ThSiO_4$, $PbTiO_3$ and YAG (Y-Al garnet: $Y_3Al_5O_{12}$) standards. Measured intensites converted to concentrations using the CITZAF matrix correction (Armstrong, 1995). O concentration determined stoichiometrically. Raw concentrations (in weight %; not shown) of U, Th, Pb, Y, and O were re-normalized to sum to 100% and then recast in ppm (values listed in table). Y*Lg* interference with the Pb*Ma* line causes Pb contents to be overestimated by ca. 35 ppm, and Th*Mb* interference with the U*Ma* line causes U contents to be overestimated by ca. 16 ppm. The concentrations listed have been corrected accordingly (see text). Analytical uncertaintes listed are at the 2σ (95%) confidence level and reflect errors due to the counting statistics only.

†† Un-normalized, Y- and Th-interference corrrected (see #) totals for each point analysis in weight percent (wt. %). In most cases, the totals are close to 100% before being re-normalized (re-normalized % totals not given; see #). Generally, the 0-3% unaccounted for may be due to trace amounts of Nd, Ra, Ce, N, He, A, and/or OH commonly present in uraninite that we did not measure (e.g. Snetsinger and Polkowki, 1977; Klein and Hurlbut, 1993). Those analyses with anomalously low totals (e.g. ≤ 96%; italicized) may also have been adversely affected by non-idealities (i.e. pits and roughness) on the polished grain surface (see Fig. 2). These points were excluded from calculation of the mean chemical date (see ##).

§§ Dates calculated using equation (1). Uncertaintes given are at the 2s (95%) confidence level. Uncertainties estimated by propagating analytical uncertainties in U, Th, and Pb concentrations through equation (1) using a modified Monte Carlo method (e.g. Anderson, 1976; Terry *et al.* , 2000; White, 2001). Calculations use the decay constants of Steiger and Jäger (1977): 0.4947e-10 yr^{-1} ($^{\infty}$Th); 9.8485e-10 yr^{-1} ($^{\infty}$U); 1.55125e-10 yr^{-1} ($^{\infty}$U).

Mean chemical date excludes both points with low totals (italicized dates; see ††) and anomalously old points (dates in plain type). Dates in boldface are those used in mean calculations. Uncertainties given are 2 standard errors of the mean chemical dates (2SE).

TABLE 2. ID-TIMS DATA AND RESULTS FOR 00KG20 u1-u4a-d & m1-2

Grain†	Mass§ (mg)	U# (ppm)	Pb# (ppm)	Th/U#	Common Pb†† (pg)	$^{206}Pb^*/^{204}Pb$§§	$^{208}Pb/^{204}Pb$##	$^{206}Pb/^{238}U$†††	$^{207}Pb/^{235}U$†††	$^{207}Pb/^{206}Pb$†††	Correlation Coefficient	$^{206}Pb/^{238}U$ Date§§§ (Ma)	±	2σ§§§ (Ma)	$^{207}Pb/^{235}U$ Date§§§ (Ma)	±	2σ§§§ (Ma)	$^{207}Pb/^{206}Pb$ Date§§§ (Ma)	±	2σ§§§ (Ma)
Uraninite																				
u1	2.5	411002	991.9	0.062	4.5	38691.3	0.020	0.002632(0.15)	0.01694(0.17)	0.04669(0.08)	0.864	16.942	±	0.025	17.058	±	0.029	33.4	±	2.0
u2	1.2	734695	1740.6	0.070	8.4	17243.4	0.023	0.002571(0.09)	0.01660(0.10)	0.04682(0.05)	0.857	16.552	±	0.015	16.713	±	0.018	39.9	±	1.3
u3	1.4	517929	1230.8	0.069	41.4	2849.6	0.022	0.002528(0.10)	0.01638(0.14)	0.04698(0.09)	0.736	16.279	±	0.017	16.497	±	0.023	48.4	±	2.3
u4a	1.2	351631	827.8	0.051	0.4	181580.6	0.017	0.002576(0.05)	0.01662(0.06)	0.04681(0.04)	0.736	16.583	±	0.008	16.742	±	0.011	39.5	±	1.0
u4b	2.5	267762	644.0	0.044	0.6	198820.6	0.014	0.002638(0.05)	0.01702(0.07)	0.04680(0.04)	0.782	16.982	±	0.009	17.139	±	0.011	39.2	±	1.0
u4c	1.2	425932	986.4	0.049	0.9	95393.5	0.016	0.002536(0.07)	0.01637(0.09)	0.04681(0.05)	0.806	16.324	±	0.012	16.483	±	0.015	39.7	±	1.3
u4d	1.2	535167	1237.8	0.054	0.6	187062.8	0.018	0.002528(0.06)	0.01632(0.07)	0.04681(0.04)	0.800	16.279	±	0.009	16.436	±	0.012	39.5	±	1.0
Monazite																				
m1	16.0	4789	56.5	10.114	100.6	156.3	3.258	0.002829(0.14)	0.01820(0.52)	0.04657(0.49)	0.382	18.21	±	0.03	18.28	±	0.10	27.4	±	11.7
m2	7.7	4272	92.8	14.867	44.9	212.3	4.673	0.004132(0.19)	0.02600(0.55)	0.04560(0.50)	0.411	26.58	±	0.05	26.04	±	0.14	-23.3	±	12.2

Notes :

† Fractions designated by mineral: m = monazite; u = uraninite. All fractions were single crystals, except for u4a-d which were single fragments of a larger crystal.

§ Sample weights, estimated using sample dimensions determed from a calibrated grided video monitor, are known to within 40% based on comparisons of estimated and measured weights.

Compositions expressed as ppm U, ppm total Pb, and Th/U. Th/U ratios calculated from the $^{208}Pb/^{206}Pb$ ratios.

†† Total common Pb in analyses.

§§ Measured ratio corrected for fractionation and spike only; Pb fractionation is 0.12 ± 0.04% per a.m.u. (atomic mass unit) for multicollector (dynamic) Faraday analyses and 0.15 ± 0.04% per a.m.u. for single collector Daly analysis based on repeated analyses of NBS-981.

Radiogenic Pb. See ††† for analytical details.

††† Isotopic ratios corrected for fractionation, spike, blank, and initial common Pb. Total procedural U blank < 0.1 pg ± 50%. Data were reduced using a total procedural Pb blank of 3.5 pg ± 50% except for analyses with < 3.5 pg total common Pb, in which case this value was used as blank and the uncertainty reduced to 20%. Pb blank composition: $^{208}Pb/^{204}Pb$ = 19.10 ± 0.1%, $^{207}Pb/^{204}Pb$ = 15.71 ± 0.1%, $^{206}Pb/^{204}Pb$ = 38.65 ± 0.1% (uncertainties at the 1σ level). Initial common Pb composition used is based on the model of Stacey and Kramers (1975) and the interpreted age of the sample. Numbers in parentheses are the % error reported at the 2σ (95%) confidence level.

§§§ Uncertainties in millions of years (Ma) at the 2σ (95%) confidence level. Age calculations based on the decay constants of Steiger and Jäger (1977): 0.4947e-10 yr^{-1} (^{232}Th); 9.8485e-10 yr^{-1} (^{235}U); 1.55125e-10 yr^{-1} (^{238}U).

TABLE 3. SUMMARY OF U-Pb-Th GEOCHRONOLOGIC RESULTS FOR 00KG20

Technique†	Mineral	Date (Ma)	±	Uncertainty (Ma)
ID-TIMS§	monazite	18.28	±	0.10
ID-TIMS#	uraninite	17.63	±	+108.72/-0.63
ID-TIMS§	uraninite	17.139	±	0.011
Chemical††	uraninite	18.17	±	0.52
Chemical§§	uraninite	17.77	±	0.59
Chemical##	uraninite	17.96	±	0.40

Notes :

† ID-TIMS = isotope-dilution, thermal ionization mass spectrometry. Chemical = electron microprobe total U-Th-Pb chemical dating.

§ Monazite ID-TIMS date is $^{207}Pb/^{235}U$ date of grain m1 (Table 2). Uraninite ID-TIMS date is $^{207}Pb/^{235}U$ date of grain u4b (Table 2). ID-TIMS uncertainties are given at the 2σ (95%) confidence level.

Upper intercept from York 2 regression (York, 1969; Ludwig, 1991) through uraninites u1-u4ad (Fig. 4b). Data corrected for ^{230}Th deficiency.

†† Transect 1 mean and 2 standard errors of the mean (Table 1).

§§ Transect 2 mean and 2 standard errors of the mean (Table 1).

All points mean and 2 standard errors of the mean (Table 1).

TABLE 4. U DIFFUSIVITY: TIME AND TEMPERATURE CALCULATIONS

	TIME			TEMPERATURE	
T† (°C)	D,§ ($cm^2 s^{-1}$)	t# (Ma)	t†† (Ma)	D,§ ($cm^2 s^{-1}$)	T§§ (°C)
	Sabioni *et al* . (1998): D_o = 8.54e-7 $cm^2 s^{-1}$. E_a = 425.54 kJ mol^{-1}.				
500	1.78E-35	4.91E+15	1	8.74E-20	1434
525	1.41E-34	6.21E+14	2	4.37E-20	1395
550	9.83E-34	8.90E+13	3	2.91E-20	1373
575	6.12E-33	1.43E+13	4	2.19E-20	1358
600	3.43E-32	2.55E+12	5	1.75E-20	1347
625	1.75E-31	5.01E+11	6	1.46E-20	1337
650	8.14E-31	1.07E+11	7	1.25E-20	1330
675	3.50E-30	2.50E+10	8	1.09E-20	1323
700	1.40E-29	6.27E+09	9	9.72E-21	1317
725	5.19E-29	1.68E+09	10	8.74E-21	1312
750	1.81E-28	4.82E+08	11	7.95E-21	1307
			12	7.29E-21	1303
			13	6.73E-21	1299
			14	6.25E-21	1296
			15	5.83E-21	1292
			16	5.47E-21	1289
			17	5.14E-21	1286
			18	4.86E-21	1284
	Yajima *et al* . (1966): D_o = 1e-4 $cm^2 s^{-1}$. E_a = 290 kJ mol^{-1}.				
500	2.56E-24	3.42E+04	1	8.74E-20	733
525	1.05E-23	8.32E+03	2	4.37E-20	713
550	3.96E-23	2.21E+03	3	2.91E-20	702
575	1.38E-22	6.33E+02	4	2.19E-20	694
600	4.48E-22	1.95E+02	5	1.75E-20	688
625	1.36E-21	6.41E+01	6	1.46E-20	683
650	3.90E-21	2.24E+01	7	1.25E-20	679
675	1.06E-20	8.27E+00	8	1.09E-20	676
700	2.72E-20	3.22E+00	9	9.72E-21	673
725	6.67E-20	1.31E+00	10	8.74E-21	670
750	1.57E-19	5.58E-01	11	7.95E-21	668
			12	7.29E-21	666
			13	6.73E-21	663
			14	6.25E-21	662
			15	5.83E-21	660
			16	5.47E-21	658
			17	5.14E-21	657
			18	4.86E-21	655

Notes :

† Reasonable temperatures, between the metamorphic temperature of the country rock (ca. 500 °C - Hurtado, 2002) and the temperature of a leucogranitic melt (ca. 700 °C – Scaillet *et al.* , 1995; Patiño Douce and Harris, 1998).

§ $D_a = D_o \exp(E_a / RT)$. D_o = diffusivity at infinite temperature (in $cm^2 s^{-1}$); E_a = activation energy (in kJ mol^{-1}); R = gas constant (8.31451 J $mol^{-1} K^{-1}$); T = temperature (in K); D_a = diffusivity (in $cm^2 s^{-1}$) at temperature T .

Required time to diffusively develop the profiles in Fig. 3a, at a given temperature (see †), based on the modeled $D_a t$ value (2.76e-6 cm^2; Fig. 5) and the appropriate Arrhenius parameters.

†† Reasonable times, between 1 Ma and the age of 00KG20 (Table 3).

Required temperature to diffusively develop the profiles in Fig. 3a, over a given period of time (see ††), based on the modeled $D_a t$ value (2.76e-6 cm^2; Fig. 5) and the appropriate Arrhenius parameters.

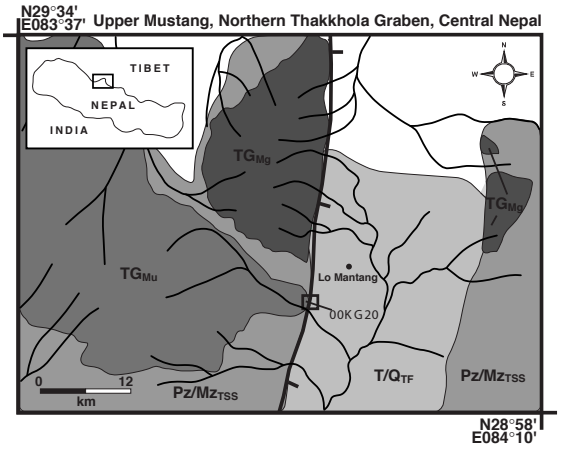

Figure 1

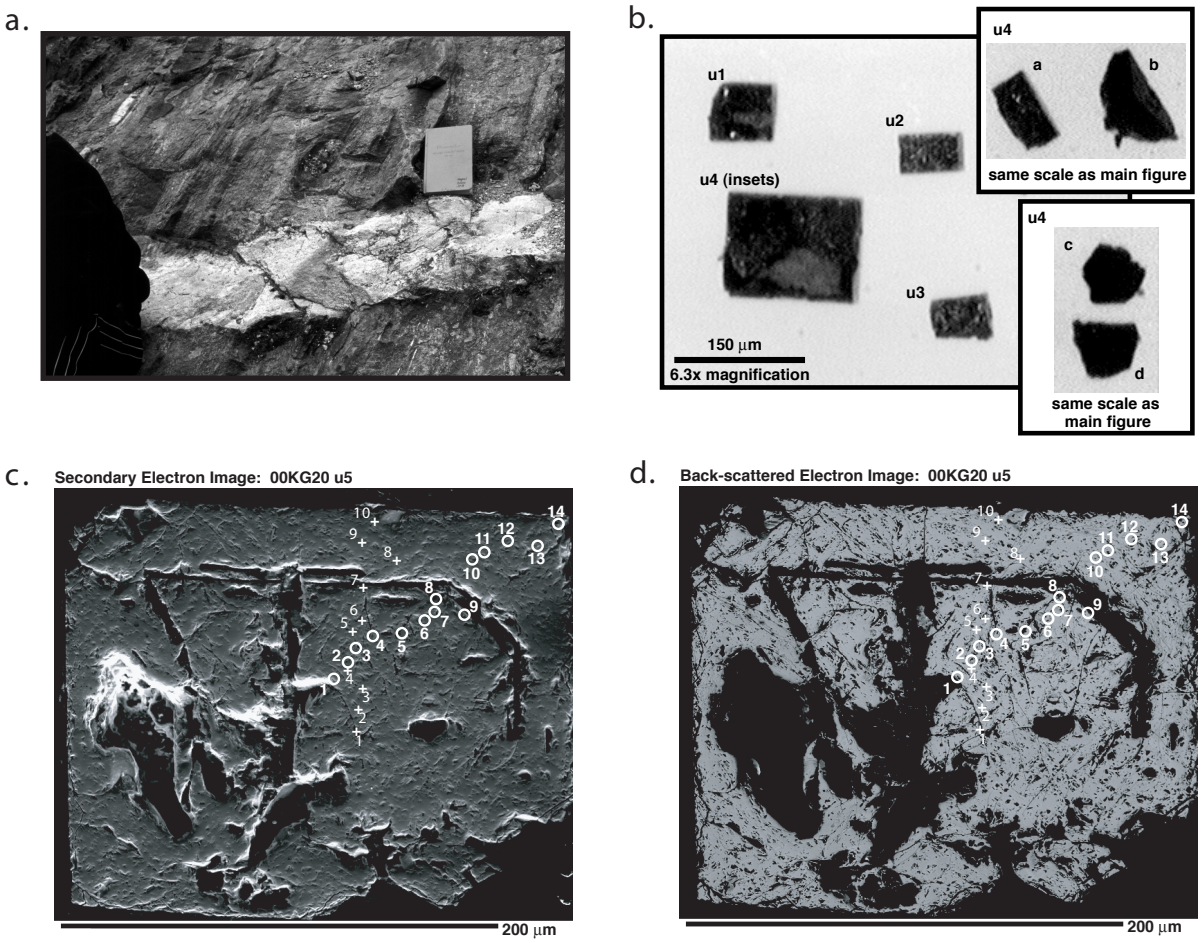

Figure 2

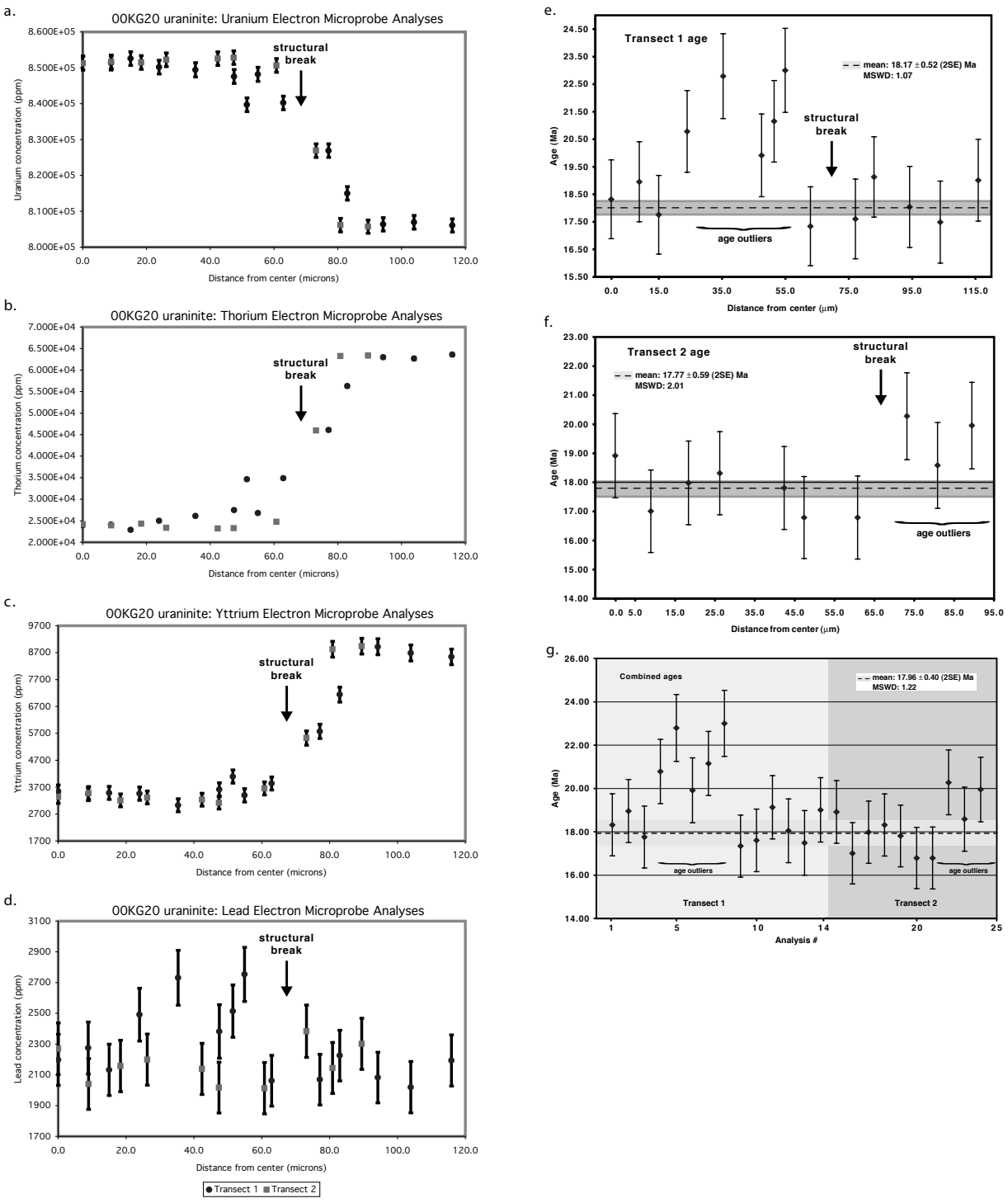

Figure 3

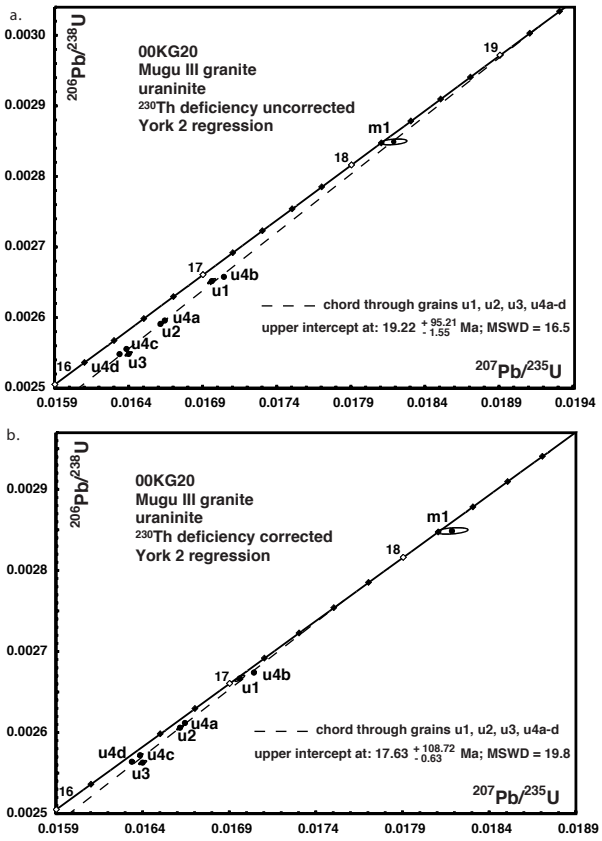

Figure 4

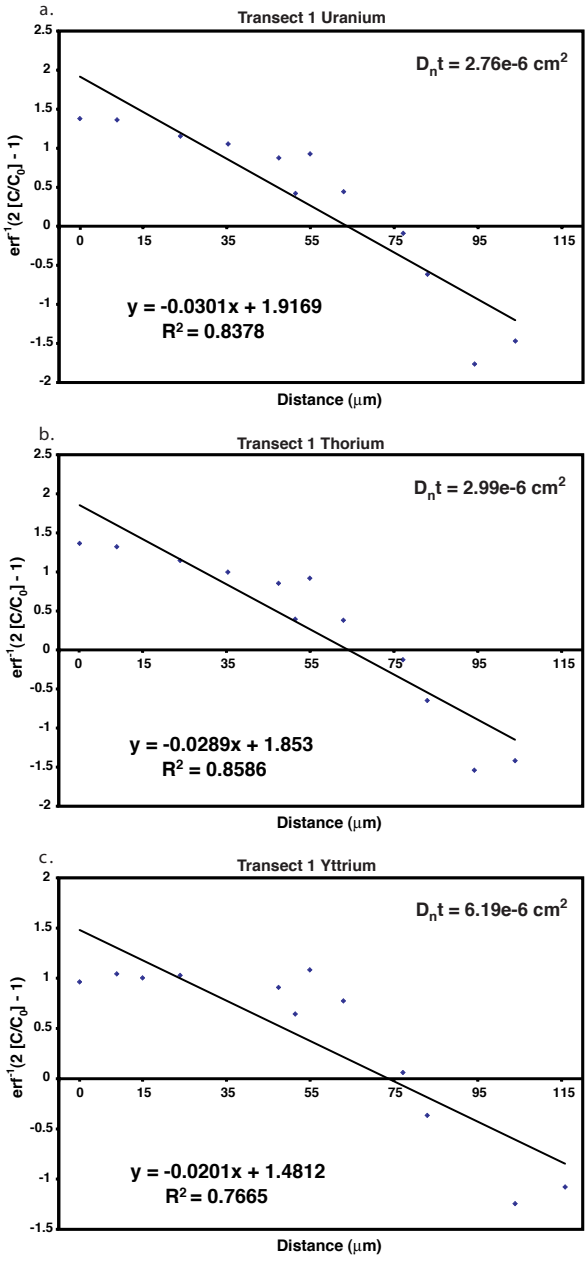

Figure 5